The final publication is available at

http://doi.org/10.1149/2.1431713jes

Additional Information

Electrochemical fabrication and characterization of p-CuSCN/n-Fe$_2$O$_3$ heterojunction devices for hydrogen production

F. Bouhjar [a, b, c], Shafi Ullah [a], M.L. Chourou[b], M. Mollar [a], B.Marí [a] and B. Bessaïs [b]

a. Institut de Disseny i Fabricació, Universitat Politècnica de València. Camí de Vera s/n 46022 València (Spain)
b. Laboratoire Photovoltaïque, Centre de Recherches et des Technologies de l'Energie Technopole de Borj – Cedria, Hammam-Lif 2050 (Tunisia)
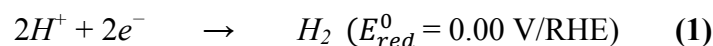*c. University of Tunis*

Abstract

p-CuSCN/n-Fe$_2$O$_3$ heterojunctions were electrochemically prepared by sequentially depositing α-Fe$_2$O$_3$ and CuSCN films on FTO (SnO$_2$:F) substrates. The α-Fe$_2$O$_3$ and CuSCN films and the α-Fe$_2$O$_3$/CuSCN heterojunctions were characterized by Field Emission Scanning Electron Microscopy (FESEM), Energy-Dispersive X-ray spectroscopy (EDX), and X-Ray Diffraction (XRD). Pure crystalline CuSCN films were electrochemically deposited on α-Fe$_2$O$_3$ films by fixing the SCN/Cu molar ratio in the electrolytic bath to 1:1.5 at 60 °C and at a potential of - 0.4 V. The photocurrent measurements showed an increase of the intrinsic surface states or defects at the α-Fe$_2$O$_3$/CuSCN interface. The photoelectrochemical performance of the α-Fe$_2$O$_3$/CuSCN heterojunction was examined by chronoamperometry and linear sweep voltammetry techniques. It was found that the α-Fe$_2$O$_3$/CuSCN structure exhibits a higher photoelectrochemical activity when compared to α-Fe$_2$O$_3$ thin films. The highest photocurrent density was obtained for α-Fe$_2$O$_3$/CuSCN films in 1 M NaOH electrolyte. This high photoactivity was attributed to the high active surface area and to the external applied bias;, which favors the transfer and the separation of the photogenerated charge carriers in α-Fe$_2$O$_3$/CuSCN heterojunction devices. The flat band potential and the donor density were found to be maximal for the heterojunction. These results suggest a substantial potential to achieve heterojunction thin films in photoelectrochemical water splitting applications.

Keywords: α-Fe$_2$O$_3$/CuSCN;Interface; Electrochemicaldeposition; Heterojunction; photocurrent; Mott-Schottky.
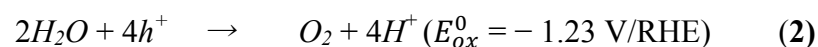
Introduction

In recent years, a great deal of attention has been paid to heterogeneous thin film deposition on highly structured semiconductor substrates such as Fe_2O_3, ZnO, TiO_2, and GaN to form heterojunction; the latter semiconductor are essential in many electrical, photoelectrical, and catalytic applications generally requiring an enlargement of the interface area. Thermodynamically, the water splitting reaction is an uphill process that requires a minimum energy of 1.23 eV as the Gibbs free energy change is $\Delta G° = 237.2$ kJ mol^{-1} or 2.46 eV per H_2O molecule [1]. However, a high overpotential is needed due to non-idealities in real operations taking into account the water splitting reaction complexity. The water splitting process requires two steps as it is not quite as straightforward as ripping apart the three atoms in H_2O. The full reaction requires the participation of two H_2O molecules, which are then separated according to the following reduction and oxidation half-reaction [2].
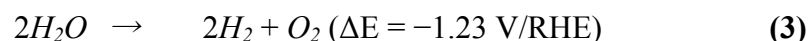
Reduction reaction:

$$2H^+ + 2e^- \quad \rightarrow \quad H_2 \ (E^0_{red} = 0.00 \text{ V/RHE}) \qquad (1)$$

Oxidation reaction:

$$2H_2O + 4h^+ \quad \rightarrow \quad O_2 + 4H^+ \ (E^0_{ox} = -1.23 \text{ V/RHE}) \qquad (2)$$

Overall reaction:

$$2H_2O \quad \rightarrow \quad 2H_2 + O_2 \ (\Delta E = -1.23 \text{ V/RHE}) \qquad (3)$$

where RHE indicates a reversible hydrogen electrode (RHE).

Given that four-electron water oxidation is the rate-limiting step in the overall water splitting reaction, the development of high-efficiency photoanodes for O_2 evolution capable of overcoming the high overpotential requiring to perform this reaction represents an important barrier that must be overcome [3]. Hematite (α- Fe_2O_3) is one of the most promising photoanode candidates as it has a narrow bandgap of ~ 2.1-2.2 eV and allows a ~ 16.0% theoretical solar-to-hydrogen (STH) efficiency for photoelectrochemical (PEC) water splitting [4,5,6]. Moreover, compared to other narrow bandgap semiconductors, α- Fe_2O_3 offers many additional advantages, including excellent stability in alkaline solutions, earth abundance, and nontoxicity [3-7]. However, α- Fe_2O_3 has extremely poor electrical conductivity with a hole diffusion length of $2 - 4$ nm [8] and suffers from a high charge carriers recombination leading to a low PEC performance; the future success of α- Fe_2O_3 photoanodes in PEC water splitting remains

questionable, as α- Fe_2O_3 itself can hardly achieve rather high PEC efficiency for practical potential use and necessitates modification to improve the PEC performance.

Herein, an overview of the synthesis, modification, and characterization of nanostructured α-Fe_2O_3 thin film is provided with an emphasis on charge carrier dynamics and PEC properties [9]. In the past few years, an increasing number of studies focused on α-Fe_2O_3 heterostructures, which incorporate the second material to promote charge separation, charge collection, and surface catalysis. Indeed, higher PEC activities have been achieved with such α-Fe_2O_3 heterostructure-based photoanodes than with their single-component counter- parts, such as WO_3/α-Fe_2O_3 [10], ZnO/ α-Fe_2O_3 [11], n-Si/ α-Fe_2O_3[12], α-Fe_2O_3 /NiO[13], α-Fe_2O_3:Ti/Cu_2O[14], p-Si/ α-Fe_2O_3 /Au[15], and α-Fe_2O_3 /Gr/$BiV_{1-x}Mo_xO_4$ [16].

Table I shows a review of the characteristics of some typical α-Fe_2O_3-based semiconducting heterojunctions that can be found in the literature. Data in Table I include the type of the heterostructure, the fabrication method, the suggested electrons and holes charge transfer and the main photoelectrical properties of these heterostructures. These data are compared with the electrochemically deposited Fe_2O_3/CuSCN heterojunction described in this work.

The CuSCN is a p-type hole-conducting material, transparent in the visible light spectrum range, having a reasonable hole conductivity ($\geq 5 \times 10^{-4} S \cdot cm^{-1}$) [17] and a good chemical stability [18]. In this work, we describe the electrochemical deposition of Fe_2O_3/CuSCN heterojunction films. CuSCN films having various compositions were deposited on smooth Fe_2O_3 surfaces. The characterization of the films was carried out using FESEM and X-ray diffraction (XRD) techniques.

Table I: Hematite-based heterostructures including fabrication methods, suggested charge transfer and photoelectrochemical characteristics.

Heterostructure	Fabrication method	Suggested charge transfer		Photoelectrochemistry	Ref
		Electron	**Hole**		
WO_3/ α-Fe_2O_3	Sol–gel	$WO_3 \rightarrow$ α-Fe_2O_3	None	Photocurrent:22μAcm^{-2} at 0.8V vs. Ag/AgCl (500 W Xe lamp) lec-trolyte: 0.2 M Na_2SO_4 (pH = 7.5)	[19]
WO_3/ α-Fe_2O_3	spin coating and Spray pyrolysis	None	None	Photocurrent:22 mAcm^{-2} at 0.8V vs. Ag/AgCl; electro-lyte: 0.05 M PBS (pH = 7)	[20]
ZnO/α-Fe_2O_3	Hydrothermal and spin coating	α-$Fe_2O_3 \rightarrow$ ZnO	ZnO $\rightarrow$ α-Fe_2O_3	Photocurrent:1.6mA cm^{-2} at 0.6V vs. Ag/AgCl; electrolyte:1 M NaOH	[21]

α-Fe$_2$O$_3$ /Gr/BiV$_{1-x}$Mo$_x$O$_4$	Hydrothermal and spin coating	BiV$_{1-x}$Mo$_x$O$_4 \rightarrow \alpha$-Fe$_2$O$_3$	α-Fe$_2$O$_3$ $\rightarrow$BiV$_{1-x}$Mo$_x$O$_4$	Photocurrent: 0.39 mA cm^{-2} at 1.5 V vs. RHE (64 mW cm^{-2} λ > 420 nm); electrolyte: 0.01 M Na$_2$SO$_4$	[22]
α-Fe$_2$O$_3$/ZnFe$_2$O$_4$	Spin coating	ZnFe$_2$O$_4 \rightarrow \alpha$-Fe$_2$O$_3$	α-Fe$_2$O$_3$ $\rightarrow$ ZnFe$_2$O$_4$	Photocurrent: 0.44 mA cm^{-2} at 0.2 V vs. Ag/AgCl; electrolyte: 0.1 M glucose and 0.5 M NaOH (pH = 13.0)	[23]
α-Fe$_2$O$_3$: Ti/ZnFe$_2$O$_4$	Hydrothermal and surface treatment	ZnFe$_2$O$_4 \rightarrow \alpha$-Fe$_2$O$_3$: Ti	α-Fe$_2$O$_3$: Ti $\rightarrow$ ZnFe$_2$O$_4$	Photocurrent: 0.3 mA cm^{-2} at 1.4 V vs. RHE; electrolyte: 1 M KOH	[24]
α-Fe$_2$O$_3$: Co/MgFe$_2$O$_4$	Hydrothermal and wet impregnation	MgFe$_2$O$_4 \rightarrow \alpha$-Fe$_2$O$_3$: Co	α-Fe$_2$O$_3$: Co $\rightarrow$MgFe$_2$O$_4$	Photocurrent: 3.34 mA cm^{-2} at 1.4 V vs. RHE; electrolyte: 0.01 M Na$_2$SO$_4$	[25]
p-CaFe$_2$O$_4$/n-Fe$_2$O$_3$	Hydrothermal and two-step annealing	p-CaFe$_2$O$_4 \rightarrow$ n-Fe$_2$O$_3$	n-Fe$_2$O$_3$ $\rightarrow$ p-CaFe$_2$O$_4$	Photocurrent: 0.53 mA cm^{-2} at 1.23 V vs. RHE; electrolyte: 1.0 M KOH (pH = 13.9)	[26]
α-Fe$_2$O$_3$: Ti/Cu$_2$O	Spray pyrolysis	Cu$_2$O $\rightarrow\alpha$-Fe$_2$O$_3$: Ti	α-Fe$_2$O$_3$: Ti $\rightarrow$ Cu$_2$O	Photocurrent: 2.60 mA cm^{-2} at 0.95 V vs. SCE (Xe lamp, 150 mW cm^{-2}); electrolyte: 0.1 M NaOH	[27]
α-Fe$_2$O$_3$/CuSCN	electrodeposition	CuSCN$\rightarrow \alpha$-Fe$_2$O$_3$	α-Fe$_2$O$_3$ $\rightarrow$ CuSCN	Photocurrent: 2.90 mA cm^{-2} at 0.59 V vs. Ag/AgCl. (Xe lamp: 150 W); electrolyte 0.1 M NaOH(pH = 13.9)	**our work**

2. Experimental details

2.1. Electrodeposition

The iron oxide films were deposited using an electrodeposition bath consisting of an aqueous solution containing ferric chloride (FeCl$_3$. 6H$_2$O, purity (p)$\geqslant$98.0), hydrogen peroxide (H$_2$O$_2$, $\geqslant$99.99%), Potassium fluoride (KF, p$\geqslant$99.97%) and Potassium chloride (KCl, p$\geqslant$99.0%). Potassium perchlorate (KClO$_4$, p$\geqslant$99.0%), Copper(II) perchlorate hexahydrate (Cu (ClO$_4$)$_2$·6H$_2$O, p$\geqslant$98.0%), Ammonium thiocyanate (NH$_4$SCN , p$\geqslant$99.0%) and triethanolamine (TEA, C$_6$H$_{15}$NO$_3$, p$\geqslant$99.5%) were used as precursors for the electrodeposition of CuSCN. All chemicals were purchased from Aldrich chemicals and used as received. The experimental set-up used to prepare α-Fe$_2$O$_3$ films consisted of a computer-controlled potentiostat/galvanostat and a classical three-electrode electrochemical cell. The electrochemical cell was filled with an electrolyte solution containing deionized water + 5mM FeCl$_3$ + 5mM KF + 1M H$_2$O$_2$ + 0.1M KCl. The working electrode (WE) is a fluorine-doped tin oxide (FTO) coated glass having a sheet resistance of 10 Ω/ ; it was previously cleaned in an ultrasonic acetone bath for 15 min

and then rinsed in distilled water and dried. Pt and Ag/AgCl electrodes were used as counter-electrode and reference electrode, respectively. The films were deposited by cathodic electrodeposition. In order to to have a thickness of approximately 500 nm for all Fe_2O_3 films, the deposition potential was fixed at - 0.1V and the debited charge was 1.2 C. The temperature of the solution was fixed at 298 K by a thermostat. After the deposition process, the films were rinsed with distilled water. To obtain the desired α-Fe_2O_3 phase, the deposited films were annealed at 650°C for 2h in air. The electrodeposition of CuSCN was performed in the same way than the Fe_2O_3 films. The deposition potential was fixed at -0.4 V and the debited charge was 1 C giving rise to a film thickness a of about 3 μm. The temperature of the solution was fixed at 333 K by a thermostatic bath. The electrolytic bath was prepared from 0.1M $KClO_4$, 0.01 M Cu $(ClO_4)_2 \cdot 6H_2O$, 0.05 M NH_4SCN and 0.06 M TEA ($C_6H_{15}NO_3$). About 0.5-1.0 mL of 2 M NH_3 was added to the electrolyte to keep the pH of the solution around 9.

2.2. Materials characterization

The crystal structure of α-Fe_2O_3 and α-Fe_2O_3/CuSCN heterojunction were investigated by XRD (Rigaku Ultima IV diffractometer in the Bragg-Bentano configuration) using the CuKα radiation (λ = 1.54060 Å). The microstructural and elemental analyses were characterized using a Zeiss ULTRA 55 model scanning electron microscope (SEM) equipped with an energy dispersive spectroscopy (EDS) system. To determine the band gap energy was estimated from the optical absorption, which was measured by recording the transmission spectra using a UV-Visible spectrophotometer (Ocean Optics HR4000) coupled to an integrating sphere (in order to collect both specular and diffuse transmittance).

The photoluminescence (PL) was measured using a He-Cd laser (λ=325 nm) and a Jobin Yvon-Horiba spectrometer coupled to a Hamamatsu back-thinned Si-CCD detector.

2.3. Photoelectrochemical and electrochemical analyses

The PEC measurements were performed in a quartz cell to facilitate the light reaching the photoelectrode surface. The light exposed surface of the working electrode is 0.25 cm^2. The electrolyte used in all PEC measurements is 1.0 M NaOH (pH = 13.6). The electrolyte was purged with nitrogen gas before the experiments in order to prevent any possible reaction with dissolved oxygen at the counter-electrode. A potentiostat/galvanostat Autolab PGSTAT302N (Metrohm, Netherlands) with a Pt rod counter-electrode and an Ag/AgCl saturated in 3 M KCl reference electrode was used. The films were illuminated with a 150 W Xenon lamp

(PLSSXE300/300UV) coupled to a chopper and a selective blue filter ($\lambda > 400$ nm). The set-up was completed with an automatic shutter and a filter box. The whole system was controlled by a homemade software. The J-V curves were monitored by linear sweep voltammetry (LSV) at 100 mV/s setting the potentiostat in the range of 0V to +0.8 V vs Ag/AgCl. The chronoamperometry curves of the films were also obtained at +0.1 V both in dark and under illumination with an intensity of about 1 SUN (100 mW cm^{-2}) at the film surface. Mott–Schottky measurements were performed using an electrochemical impedance analyzer in the three-electrode configuration in a 0.1 M NaOH electrolyte solution; the AC amplitude was 10 mV and the frequency was in the 100 kHz - 0.1 Hz range. The flat band potential (V_{fb}) and the donor density (N_D) were determined in the dark from the impedance measurements.

3. Results and discussion

Figure 1 shows a schematic cross-sectional view of the α-Fe$_2$O$_3$/CuSCN heterojunction deposited on FTO glass substrates.

3.1. Potential variation

Figure 2.a shows the cyclic voltammogram of the Fe$_2$O$_3$ films recorded at 50 mV/s. During the negative sweeps Fe^{3+} was reduced to Fe. In the reduction region, the film is deposited at a potential ranging between -0.2 and 0 V. These films showed negligible photo-activity and were not further characterized [28]. Furthermore, in the positive sweep the films were deposited by an electrochemical oxidation of the Fe^{2+} ions to Fe^{3+} ions followed by precipitation of Fe^{3+} ions as ferric hydroxide (Fe (OH)$_3$). The anodic deposition of the Iron oxide is represented by the following equations [29].

$$Fe^{2+} \leftrightarrow Fe^{3+} + e^{-} \qquad \textbf{(4)}$$

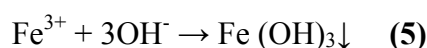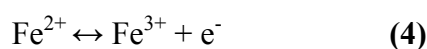$$Fe^{3+} + 3OH^{-} \rightarrow Fe\,(OH)_3\downarrow \quad \textbf{(5)}$$

Figure 2. b shows a cyclic voltammogram performed at 200mV/s onto a α-Fe$_2$O$_3$ electrode using the electrolytic solution described in the experimental section. The voltammetric scan was initiated at 0 V towards the negative direction of up to -0.8 V. The cathodic threshold potential for the reduction of Cu^{2+} to Cu^{+} ions in the solution is about -0.20 V. The cathodic current increases slowly to -0.40 V, then steeply up to -0.60V, and then becomes almost constant. The initial slow increase of the current indicates the existence of Cu(II)-TEA complexes in the solution that results in slow diffusion leading to a shift of the reduction

potential to more negative values as well as small cathodic reaction current density [30]. The electrodeposition of CuSCN is manifest when a white film appears on the electrode surface at about -0.30V and subsequently grows rapidly as the potential increases up to -0.60 V, which is referred to as the kinetically controlled region. In the potential range -0.60 to -0.80 V, the saturation current density indicates that the diffusion process reachesc a limit accompanied with a minor co-deposition of copper. Small brown spots are observed in the film when the deposition potential was above -0.60 V. The voltammetric scan from -0.80 to 0.40V shows a sharp peak at about -0.20 V, which means that the CuSCN layer acts as a passivating layer for the α-Fe$_2$O$_3$ electrode. Another maximum around 0.30 to 0.40 V is related to the oxidation of Cu$^+$ to Cu^{2+} ions. Hence, the growth process of the CuSCN film from the TEA chelated aqueous solution suggests that the cupric ions related to the Cu(II)-TEA complexes and stabilized in the electrolyte solution, were first reduced to cuprous ions (Cu^{2+}+e$^-$→Cu$^+$), and then the CuSCN film forms from the reaction between cuprous ions and thiocyanate ions (Cu$^+$ + SCN$^-$→ CuSCN). Such a deposition takes place in a potential ranging between -200 and -550 mV. Thereafter, Cu codeposition would occur. Hence, one may conclude that the appropriate deposition potentials in the sole deposition of CuSCN in the TEA-chelated aqueous solution should be selected in the potential range of -200 to -550 mV. To further study the influence of the composition of the electrolytic bath on the nucleation and growth of the CuSCN films electrodeposited on the α-Fe$_2$O$_3$ surface, chronoamperometry measurements based on current transient recorded during the electrodeposition process at -0.40 V were performed. Figure 3 shows the chronoamperometry for a CuSCN film depositesd from an electrolyte containing Cu and SCN in the molar proportion of 1:1.5. The rapid surge in the current density observed at the onset of the applied potential is due to the double layer charging, and then, the current density decayed gradually due to an increase in the electric resistance of the electrochemical system related to nucleation and growth of CuSCN crystals having semiconductor characteristics [31]. After an interval of about 200 s, there is a gradual increase of the current density for a period of time and then the current density becomes constant.

3.2. Morphological, chemical composition and structural characterizations

Figures 4a and 4b display the FESEM images of the CuSCN and the α-Fe$_2$O$_3$ films deposited on FTO substrates, respectively. FESEM image of CuSCN (Figure 4a) shows a mixture of leafy and intrinsic trigonal pyramid shapes with some dispersion in the grain sizes. Figure 4b shows the morphology of the α-Fe$_2$O$_3$ films, revealing nanostructured grains having a size dimension of about 20 nm. Figures 4 c and 4d show the CuSCN films deposited on α-Fe$_2$O$_3$ covered substrates at different magnifications. For CuSCN films deposited on α-Fe$_2$O$_3$ only trigonal pyramid shapes with bigger grain sizes of approximately 3 μm are observed. On the other hand, one may notice that the grain size of CuSCN films deposited on α-Fe$_2$O$_3$ are greater than those deposited on FTO.

Figure 5 shows vertical cross section images of α-Fe$_2$O$_3$ (Figures 5 a-b), CuSCN (Figure 5c) and α-Fe$_2$O$_3$/CuSCN (Figure 5d) thin films deposited on FTO glass. The thickness of the α-Fe$_2$O$_3$ films is about 500 nm and that of the CuSCN layer is about 3.7 μm. Figure 5d shows a cross-sectional FESEM image of the complete device (FTO/α-Fe$_2$O$_3$/CuSCN). The overall thickness between the border of the FTO layer and the top of the CuSCN layer corresponding to the α-Fe$_2$O$_3$/CuSCN heterojunction is about 4. 2 μm. The stoichiometric proportions of the CuSCN films prepared in an electrolyte solution having a molar ratio [Cu^{2+}]/[SCN$^-$] of 1:1.5 at a static potentialof -400 mV and a temperature of 333 K were estimated by EDX analyses. Figures 6a and 6b show EDX emental analyses of the electrodeposited α-Fe$_2$O$_3$ and CuSCN, respectively. The line observed at 0.72 keV corresponds to the L line of Fe, while the oxygen K line is peaking at 0.525 keV. The calculated atomic ratio of Fe and O is approximately equal to 2:3, which well agrees with the stoichiometric composition of α-Fe$_2$O$_3$. The percentages of the elements calculated from the EDX spectra are shown in the inset of figure 6a. Figure 6b shows the EDX spectrum of the electrodeposited CuSCN film; only lines corresponding to Cu, S, C and N are observed. The inset in Figure 6b displays the calculated percentages for the elements of the CuSCN film. The content of S in CuSCN film represents the SCN content in the film, as S is not provided from environmental impurities. It is reported in the literature that when SCN is in stoichiometric excess, Cu(SCN)$_{(1+x)}$ would show p-type semiconductor characteristics [32]. It may be pointed out that the composition of the films in the above reference [32,33] is determined from the X-ray photoelectron spectroscopy (XPS) technique. In the XPS technique, only the composition of the surface is determined, which is released from the excess of SCN ions during the growth of the film, and it is very likely that some SCN ions might have been adsorbed on the surface, and consequently XPS analysis would show a stoichiometric

excess of SCN. However, in the work of Zang et al. [34], the composition of the film determined by EDX analysis showed a stoichiometric excess of copper and still the films behaved like a p-type semiconductor like of that prepared herein. These results are confirmed by Mott–Schottky measurements performed on these samples, which reveal the p-type behavior of the electrodeposited CuSCN films (See Figure 14 b). Figure 7 shows the XRD patterns of the Fe_2O_3 and CuSCN layers deposited on FTO substrates. The XRD patterns of the Fe_2O_3/CuSCN bilayer and the FTO substrates are also shown. The XRD peaks of the α-Fe_2O_3 films are observed at $2\theta = 24.1°$, $33.1°$, $35.6°$, $40.9°$, $49.4°$, $54.0°$ and $64°$, which correspond to the (012), (104), (110), (113), (024), (116) and (300) planes of the hematite phase, respectively. The dominant peaks are associated to the (104) and (110) planes. The diffraction peaks of the trigonal structure of the α-Fe_2O_3 matches well with the reference pattern JCPDS card file n°33-0664, which corresponds to the space group R3c (167) with lattice parameters a = b = 5.03 nm and c = 13.74 nm.

It is well known that CuSCN exists in two polymorphic forms, α and β, where the β form is commonly available and more stable [35,36]. β-CuSCN has a hexagonal crystal structure where layers of SCN ions separate Cu cation planes and strong three-dimensionally Cu–S bonds interconnect these layers. For the CuSCN films, all diffraction peaks can be well indexed to the trigonal-phase β-CuSCN (space group R3m, n° 160). Compared with the standard diffraction pattern of CuSCN (JCPDS card file no. 29-0581), no specific peaks related to other phases of CuSCN or impurities can be observed, indicating a high purity and crystallinity of the final products. For the Fe_2O_3/CuSCN bilayer, all peaks match the Fe_2O_3 and CuSCN patterns except those marked with asterisks that come from the FTO substrate.

3.3. Optical properties of CuSCN

Figure 8a and 8b show the transmission and absorption spectra of the CuSCN film and the α-Fe_2O_3, respectively. The energies of the optical bandgaps can be determined from the the transmission spectra [37]. The transmittance spectrum of CuSCN (Figure 8a) shows a high optical transmission value above 60% in the visible range. A significant increase in the absorption below 320 nm can be assigned to the intrinsic band gap absorption of CuSCN. It appears that α-Fe_2O_3 films have a high absorbance in the visible region, indicating their applicability as an absorbing material [38](Figure 8b). To calculate the optical band-gap energy (E_g) of the films, the absorption coefficient can be estimated as follows:

$$\alpha = \frac{1}{d} \ln \left(\frac{1}{T}\right) \qquad (6)$$

The relation between the absorption coefficient α and the energy of the incident light $h\nu$ is given by [39]:

$$\alpha h\nu = A (h\nu - E_g)^n \qquad (7)$$

where α is the absorption coefficient, A is a constant, h is the Planck's constant, ν is the photon frequency, E_g is the optical band gap, and n is equal to 2 for direct transition, and to 1/2 for indirect transition. According to the Tauc plot (($\alpha h\nu)^2$ vs.$h\nu$) (Fig. 9), the optical band gap E_g of the typical CuSCN film is about 3.3 eV. Jaffe et al.[40] predicted the existence of an indirect bandgap of 3.5 eV from an electronic band structure model calculated using the density functional theory, although absorption measurements performed on CuSCN samples indicated the presence of an indirect bandgap of 3.9 eV.

Figure 9 depicts the Tauc plot of α-Fe_2O_3 films. One may point out a direct band gap energy of about 2.1 eV, which is smaller than that of bulk α-Fe_2O_3 (2.3 eV) [41].

Figure 10 shows the normalized photoluminescence (PL) spectra for α-Fe_2O_3 and CuSCN films and for the α-Fe_2O_3/CuSCN bilayer, the excitation wavelength is the 325 nm of a He-Cd laser. The PL spectrum of the α-Fe_2O_3 shows a wide PL peak centered around 623 nm with a Full Width at Half Maximum (FWHM) of about 100 nm. The PL spectrum of CuSCN exhibits a broad band centered at 590 nm and slightly shifted to higher energy as compared to α-Fe_2O_3. Radiative transitions in CuSCN would involve deep levels (located near the middle of the gap) because the energy of the emitted photons is approximately half of the band gap energy. The PL spectrum of the Fe_2O_3/CuSCN bilayer is indistinguishable of the PL spectrum of α-Fe_2O_3. Fig 11a depicts a scheme of the energy band diagram corresponding to α-Fe_2O_3 and CuSCN before and after the formation of the heterojunction. This scheme is useful to explain the PL behaviors. Radiative recombination mainly takes place in the Fe_2O_3 layer, which means that instead of recombining through CuSCN deep levels the photoelectrons generated in the CuSCN layer move to Fe_2O_3 where they recombine radiatively. As a result, the PL spectrum of the Fe_2O_3/CuSCN heterojunction does not show any recombination in the CuSCN layer.

3.4. Photoelectrochemical measurements

3.4.1. Current voltage characteristics

The nanostructured α-Fe_2O_3 and CuSCN films, and the α-Fe_2O_3/CuSCN heterojunction, were used as photoelectrodes in a photoelectrochemical cell, and current-voltage characteristics were recorded under dark and illumination. The externally applied bias was varied from 0V vs Ag/AgCl (cathodic bias) to 0.8 V vs Ag/AgCl (anodic bias).

Figure 12 shows the photocurrent density versus applied potential for all films. For the CuSCN films, the photocurrent slightly increases for potentials over 0.4 V and then remains constant up to 0.8V. For α-Fe$_2$O$_3$, the photocurrent continuously increases for potentials above 0.55 V. In the case of the α-Fe$_2$O$_3$/CuSCN heterojunction (Fig.12) the current density in the dark is negligible in all the potential range, while under illumination the photocurrent starts increasing continuously with the applied potential from 0.2 V; it is always higher than that observed for Fe$_2$O$_3$ and CuSCN independently. Both α-Fe$_2$O$_3$ and the α-Fe$_2$O$_3$/CuSCN heterojunctions behave like photoanodes under illumination. The photocurrent density exhibited by the α-Fe$_2$O$_3$/CuSCN heterojunction may be due to improved visible light absorption and to an efficient separation of the photogenerated charge carriers (Fig.11a).

A proposed mechanism for the enhanced photocurrent density heterojunction α-Fe$_2$O$_3$/ CuSCN sample can be described as follows: under visible light irradiation, both α-Fe$_2$O$_3$ and CuSCN could be excited; in that case an electron transfer occurs from the CuSCN conduction band to that of the α-Fe$_2$O$_3$, which in turn may lead to hydrogen production at the counter-electrode. This transfer process is thermodynamically favorable since the valence and conduction bands in CuSCN become more negative than that of the α-Fe$_2$O$_3$ band levels, which in turn enhances the separation of the photogenerated charge carriers. After an initial decay in the photocurrent observed in the first illumination cycle the photocurrent tends to keep constant under long-term illumination that means an effective charge separation inside the α-Fe$_2$O$_3$/CuSCN heterojunction. A similar type of band positioning and charge carrier movement has also been reported earlier in case of TiO$_2$/Si [42], CuO/ZnO [43], CuFe$_2$O$_4$/TiO$_2$[44], Bi$_2$O$_3$/BiVO$_4$[45], and MoS$_2$/CdS [46].

The measurements of the photocurrent under pulsed light were acvhieved using a chronoamperometry technique (Fig. 13.a). In the steady state, the α-Fe$_2$O$_3$/FTO electrode shows a photocurrent density f about 5μA/cm^2. However, the α-Fe$_2$O$_3$/CuSCN/FTO heterojunction shows a photocurrent density of about 15 μA/cm^2, which is 3 times bigger than that of the α-Fe$_2$O$_3$/FTO electrode. Figure 13b shows the variation of the photocurrent density versus elapsed time during switch on/off of light for both α-Fe$_2$O$_3$/FTO and α-Fe$_2$O$_3$/CuSCN/FTO electrodes. The photocurrent density drops in the first two cycles and then was steady and quasi-reproducible after several on–off cycles of light, with no overshoot at the beginning or the end of the on–off cycle, indicating that the direction of the electron diffusion is free from grain boundaries, which can create traps to hinder electron movement and slow down the photocurrent generation[47].

It is believed that deposition of CuSCN on α-Fe₂O₃ enhanced the photoactivity of the photoanode in two aspects: (i) the p–n junction can effectively extract holes and separate charge carriers, leading to enhanced photocurrent, and (ii) The loading of the heterojunction photoanode with CuSCN further facilitates the electron transfer at the electrode/electrolyte interface and thus enhances the photoelectrochemical water oxidation.

To validate the energy band diagram suggested in Figure 11, we have made additional measurements of the photocurrent generated by the heterostructure under illumination with a wavelength that excites only the hematite ($\lambda > 400$ nm). Figure 13c shows the photocurrent generated by the α-Fe₂O₃/CuSCN heterostructure under white light illumination and under light illumination with $\lambda > 400$nm. When using white light both α-Fe₂O₃ and CuSCN are exited and the charge transfer is that shown in Figure 11 (b); holes generated in the hematite are transferred to the valence band of the CuSCN and photogenerated electrons in the CuSCN are transferred to α-Fe₂O₃. When illuminating at wavelengths higher than 400 nm ($\lambda > 400$ nm) only the hematite part is excited and the measured photocurrent is due to the charge transfer from α-Fe₂O₃ to CuSCN. As expected the photocurrent is lower in this case because the charge transfer from CuSCN to α-Fe₂O₃ has not been activated.

3.4.2. Mott–Schottky analysis

The Mott–Schottky plot ($1/C^2$ vs applied potential) was obtained and analyzed for all the samples. The flat band potential is an important physical property as regard to the performance of the material in photoelectrochemical water splitting. Both N_D and E_{fb} were estimated from the Mott-Schottky equations (Eqs. 8 and 9) [48]:

$$\frac{1}{C_{SC}^2} = \frac{2}{e\,\varepsilon\,\varepsilon_0 N_D A_S^2}\left(E - E_{fb} - \frac{KT}{e}\right) \text{ for n-type semiconductor} \qquad (8)$$

$$\frac{1}{C_{SC}^2} = -\frac{2}{e\,\varepsilon\,\varepsilon_0 N_D A_S^2}\left(E - E_{fb} + \frac{KT}{e}\right) \text{ forp-type semiconductor} \qquad (9)$$

where, e is the electron charge, ε is the dielectric constant of the semiconductor, ε_o is the vacuum permittivity, A_S is the surface area of the working electrode, k is the Boltzmann's constant, and T the temperature. The positive slopes confirm that α-Fe₂O₃ is a n-type semi-conducting material, and the negative slopes indicate that the CuSCN is a p-type semi-conducting material. The calculated donor density increases from $1.6 \cdot 10^{21}$ cm⁻³ for the α-Fe₂O₃ photoanode to $2.8 \cdot 10^{21}$ cm⁻³ for α-Fe₂O₃/CuSCN. By taking the x-axis intercept of the linear fit to the Mott-Schottky plots, the flat band potential was estimated to be -0.14 V vs Ag/AgCl for the α-Fe₂O₃

photoanode, and to -0.64V vs Ag/AgCl for the α-Fe$_2$O$_3$/CuSCN heterojunction (Fig. 14a and 14c).

4. Conclusions

Semiconducting materials such as n-Fe$_2$O$_3$ and p-CuSCN were successfully electrodeposited on FTO substrates. Chelating agents and a weak basic electrolyte solution of NH$_3$were used to avoid acidic etching of the α-Fe$_2$O$_3$. This enables us to study the energetic behavior of both semiconductors and the n-Fe$_2$O$_3$/p-CuSCN heterojunction performances as regard to photoelectrochemical applications. FESEM shows that CuSCN can easily grow thicker to cover the α-Fe$_2$O$_3$ substrate. EDX analyses revealed that CuSCN films have a slight excess of copper. The photoelectrochemical performance of the nanostructured α-Fe$_2$O$_3$/CuSCN heterojunction is higher than that of FTO/α-Fe$_2$O$_3$ and FTO/CuSCN. A maximum photocurrent density of 2.9 mA/cm^2 at 0.59 V versus Ag/AgCl was exhibited for the α-Fe$_2$O$_3$/CuSCN photoelectrode. The improvement of the photocurrent density is attributed of two major combined factors: (i) generation of an electric field in the heterojunction that suppresses the recombination of photogenerated charge carriers and (ii) application of an adequate external bias favoring the transfer and separation of the photogenerated charge carriers in the α-Fe$_2$O$_3$/CuSCN heterojunction. Enhancement in the photocurrent density has also been attributed to an appropriate band edge alignment of the semiconductors that enhances light absorption in both semiconductors.

Acknowledgements

References

[1]R. Brimblecombe, G. Charles Dismukes, Gerhard F. Swiegers and Leone Spiccia, Molecular water-oxidation catalysts for photoelectrochemical cells, Journal Homepage, Dalton Transactions, (43), 9374-9384,(2009).

[2]M. S. Prévot and K. Sivula, Photoelectrochemical Tandem Cells for Solar Water Splitting J. Phys. Chem. C 117 17879–17893(2013).

[3]A. Valdés, J. Brillet, M. Grätzel et al., Solar hydrogen production with semiconductor metal oxides: new directions in experiment and theory Phys. Chem. C hem. Phys , 14 , 49–70,(2012).

[4]A. B.Murphy, P. R. F.Barnes, L. K. Randeniya, I. C. Plumb, Grey, M. D. Horne, &J. A Glasscock, Efficiency of solar water splitting using semiconductor electrodes. International Journal of Hydrogen Energy, 31(14), 1999-2017, (2006).

[5]Z.B. Chen, T. F. Jaramillo, T. G. Deutsch, A. Kleiman-Shwarsctein, A. J. Forman, N. Gaillard, R. Garland, K. Takanabe, C. Heske, M. Sunkara, E. W. McFarland, K. Domen, E. L. Miller, J. A. Turner and H. N. Dinh, J. Mater. Res, 25, 3, (2010).

[6]K. Sivula, F. L. Formal, M. Grätzel, Solar water splitting: progress using hematite (α-Fe_2O_3)photoelectrodes.ChemSusChem, 4, 432−449,(2011).

[7]T.W. Hamann, Splitting water with rust: hematite photoelectrochemistry, Dalton Trans., 41,7830−7834,(2012).

[8]J.H.Kennedy, & K. W. Frese, Photooxidation of water at α-Fe_2O_3 electrodes. Journal of the Electrochemical Society, 125(5) 709-714, (1978).

[9] A.W. Damon, W. Gongming, L.Yichuan, L.Yat and Z. Z.Jin, Nanostructured hematite: synthesis, characterization, charge carrier dynamics, and photoelectrochemical properties Energy Environ. Sci. 5,6682−6702,(2012).

[10] K. Sivula, F. L. Formal and M. Gra¨tzel, Chem. Mater., 2009, 21, 2862–2867.

[11] Y.-K. Hsu, Y.-C. Chen and Y.-G. Lin, ACS Appl. Mater. Interfaces, 2015, 7, 14157–14162.

[12] M. T. Mayer, C. Du and D. Wang, J. Am. Chem. Soc., 2012, 134, 12406–12409.

[13]J. Li, F.Meng, S. Suri, W. Ding, F.Huang and N. Wu, Chem.Commun.,2012,48, 8213–8215.

[14] D. Sharma, S. Upadhyay, A. Verma, V. R. Satsangi, R. Shrivastav and S. Dass, Thin Solid Films, 2015, 574, 125–131.

[15] X. Wang, K.-Q. Peng, Y. Hu, F.-Q. Zhang, B. Hu, L. Li, M. Wang, X.-M. Meng and S.-T. Lee, Nano Lett., 2014, 14,

18–23.

[16] Y. Hou, F. Zuo, A. Dagg and P. Feng, Nano Lett., 2012, 12, 6464–6473.

[17]*B.O'Regan, & D.T. Schwartz Efficient Photo-Hole Injection from Adsorbed Cyanine Dyes into Electrodeposited Copper(I) Thiocyanate Thin Films Chem Mater 7,1349–1354,(1995).*

[18]*L.B.Wang, B.L. Kang, P. Wang,Y. Qiu, Review of recent progress in solid-state dye-sensitized solar cells Sol Energ Mater SolCell 90,549–573,(2006).*

[19] *W. Luo, T. Yu, Y. Wang, Z. Li, J. Ye and Z. Zou, J. Phys. D: Appl. Phys., 2007, 40, 1091–1096.*

[20] *F. Boudoire, R. Toth, J. Heier, A. Brauna and E. C. Constable, Energy Environ. Sci., 2014, 7, 2680–2688.*

[21] *Y.-K. Hsu, Y.-C. Chen and Y.-G. Lin, ACS Appl. Mater. Interfaces, 2015, 7, 14157–14162.*

[22]*Y. Hou, F. Zuo, A. Dagg and P. Feng, Nano Lett., 2012, 12, 6464–6473.*

[23] *Y. Guo, Y. Fu, Y. Liu and S. Shen, RSC Adv., 2014, 4, 36967–36972.*

[24] *C. Miao, S. Ji, G. Xu, G. Liu, L. Zhang and C. Ye, ACS Appl. Mater. Interfaces, 2012, 4, 4428–4433.*

[25] *Y. Hou, F. Zuo, A. Dagg and P. Feng, Angew. Chem., Int. Ed., 2013, 52, 1248–1252.*

[26] *M. G. Ahmed, T. A. Kandiel, A. Y. Ahmed, I. Kretschmer, F. Rashwan and D. Bahnemann, J. Phys. Chem. C, 2015, 119, 5864–5871*

[27] *D. Sharma, S. Upadhyay, A. Verma, V. R. Satsangi, R. Shrivastav and S. Dass, Thin Solid Films, 2015, 574, 125–131.*

[28]*L. P. Wen, Y. J.Guo,S.H.I Zhi-qiang, H. Hua, L. Lang, Z. Yong-Nan, L. Guo-Dong and Z. Yong-cun, Preparation and Supercapacitive Properties of Fe$_2$O$_3$/Active Carbon Nanocomposite,s chem. res. chinese universities 28(5) ,780-783,(2012).*

[29]*W. Mao-Sung, and L. Rung-Hau, Electrochemical Growth of Iron Oxide Thin Films with Nanorods and Nanosheets for Capacitors, J. Electrochem. Soc. 156, A737,(2009).*

[30]*N.Yong, J. Zhengguo, Y. F. wand J. Am. Ceram. Soc., 90 [9], 2966–2973,(2007).*

[31]*B. Debasis,C.K. Suresh, M.C. Matthew, and SudiptaSeala, In situ synthesis of carbon nanotubes decorated with palladium nanoparticles using arc-discharge in solution method J. Phys. Chem. B 108, 556,(2004).*

[32] *K. Tennakone,A. H. Jayatissa SAN Fernando,S. Wickramanayake,S. Punchihewa,L. K. Weerasena,W. D. R. Premasiri,Semiconducting and Photoelectrochemical Properties of n- and p-Type β-CuCNS, Phys Stat Sol (a) 103,491–497,(1987).*

[33]*Ni, Yong, Zhengguo Jin et Yanan Fu ."Electrodeposition of p-type CuSCN thin films by a new aqueous electrolyte with triethanolamine chelation." Journal of the American Ceramic Society 90.9 (2007): 2966-2973.*

[34]*Q. Zang, H.Guo, Z. Feng, L. Lin, J. Zhou, Z .Lin, ElectrochimActa, 55(2010) 4889–4894.*

[35]D. L .Smith, V.J .Saunders,ActaCrystallogr B 37,1807–1814,(1981).

[36]J.E.Jaffe, T.C. Kaspar, T.C. Droubay, T.Varga, M.E. Bowden, G.J. Exarhos, J Phys Chem C 114,9111–9117(2010).

[37] P. Pattanasattayavong, N.Yaacobi-Gross, K. Zhao, G. O. N. Ndjawa, Li J, F. Yan, B. C. O'Regan, A. Amassian and T. D.Anthopoulos, Hole-transporting transistors and circuits based on the transparent inorganic semiconductor copper(I) thiocyanate (CuSCN) processed from solution at room temperature. Adv. Mater. 25,1504–9,(2013).

[38]A. A. AKl Applied science 233, 307-319,(2004).

[39]L. Dghoughi, B. Elidrissi,C. Bernède, M. Addou, M. Alaouilamrani,M. Regragui,H. Erguig, Applied surface sciences 253 ,1823-1829,(2006).

[40] J. E.Jaffe, T. C.Kaspar, T .C. Droubay, T. Varga, M. E. Bowden and G. J. Exarhos, Electronic and defect structures of CuSCN J. Phys. Chem. C 114,9111–7,(2010).

[41]M.R.Belkhedkar, A.U.Ubale; International journal of Materials and chemistry,4(5) ,109-116,(2014).

[42]D.Sharma,S.Upadhyay,V.R.Satsangi,R.Shrivastav,S. Dass, Improvedphotoelectrochemical water splitting performance of $Cu_2O/SrTiO_3$ heterojunction photoelectrode, J. Phys. Chem. C 118,25320,(2014).

[43]K.K. Baek, H.L. Tuller, Atmosphere sensitive CuO/ZnO junctions, Solid State Ionics 75, 179,(1995).

[44]A. Kezzim, N. Nasrallah, A. Abdi, M. Trari, Visible light induced hydrogen on the novel hetero-system $CuFe_2O_4/TiO_2$, Energy Convers. Manag. 52, 2785,(2011).

[45]L. Chen, Q. Zhang, R. Huang, S.F. Yin, S.L. Luo, C.T. Au, Porous peanut-like Bi_2O_3-$BiVO_4$ composites with heterojunctions: one-step synthesis and their photocatalytic properties, Dalton Trans. 41, 9513,(2012).

[46]L.Ying, X. Y.Yu, W.D. Zhang, MoS_2/CdS heterojunction with high photoelectrochemical activity for H_2 evolution under visible light: the role of MoS_2, J. Phys. Chem. C 117,12949, (2013).

[47] M. Sookhakian, Y.M. Amin, S. Baradaran, M.T. Tajabadi, A. MoradiGolsheikh, W.J. Basirun, Thin Solid Films 552,204–211,(2014).

[48] G. Rahman, O.S. Joo, Electrodeposited nanostructured a-Fe_2O_3 thin films for solar water splitting: Influence of Pt doping on photoelectrochemical performance; Materials Chemistry and Physics 140, 316-322,(2013).

Figure Captions

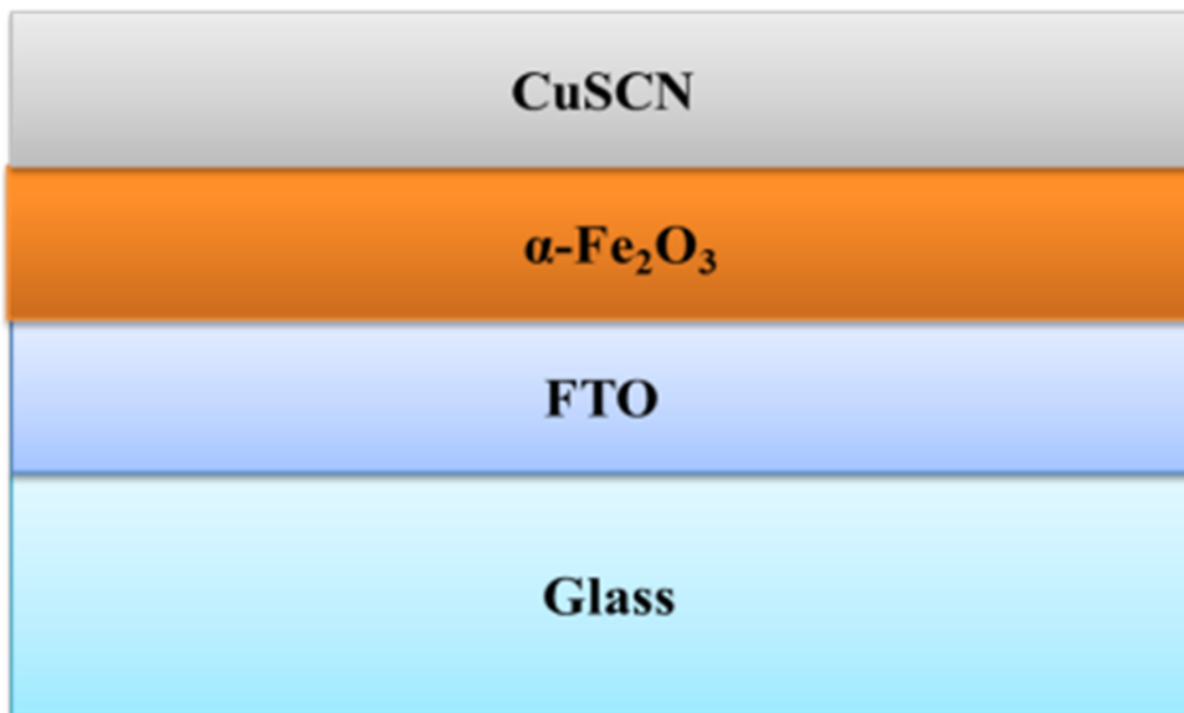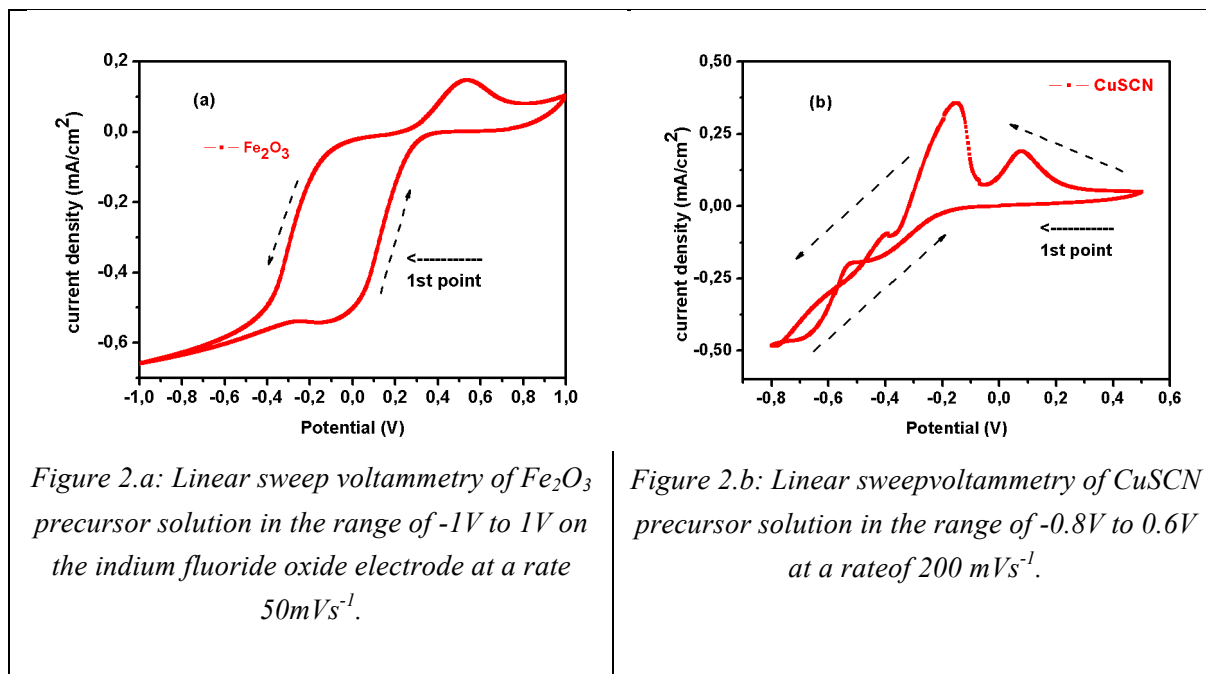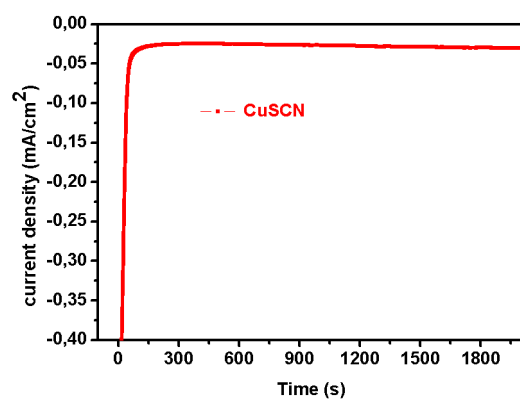Figure 1: Schematic cross-sectional view of heterojunction: FTO glass, compact α-Fe_2O_3, and CuSCN (HTM).

Figure 2.a: linear sweep voltammetry of Fe_2O_3 precursor solution in the range of -1V to 1V on the indium fluoride oxide electrode at a rate 50mVs-1.

Figure 2.b: linear sweep voltammetry of CuSCN precursor solution in the range of -0.8V to 0.6V at a rate of 200 mVs^{-1}.

Figure 3: Chronoamperometry of CuSCN with a Cu: SCN ratio of 1:1.5.

Figure 4: FESEM images for (a) CuSCN (b) α-Fe_2O_3 (c) α-Fe_2O_3/CuSCN (1μm) (d) α-Fe_2O_3/CuSCN (10μm).
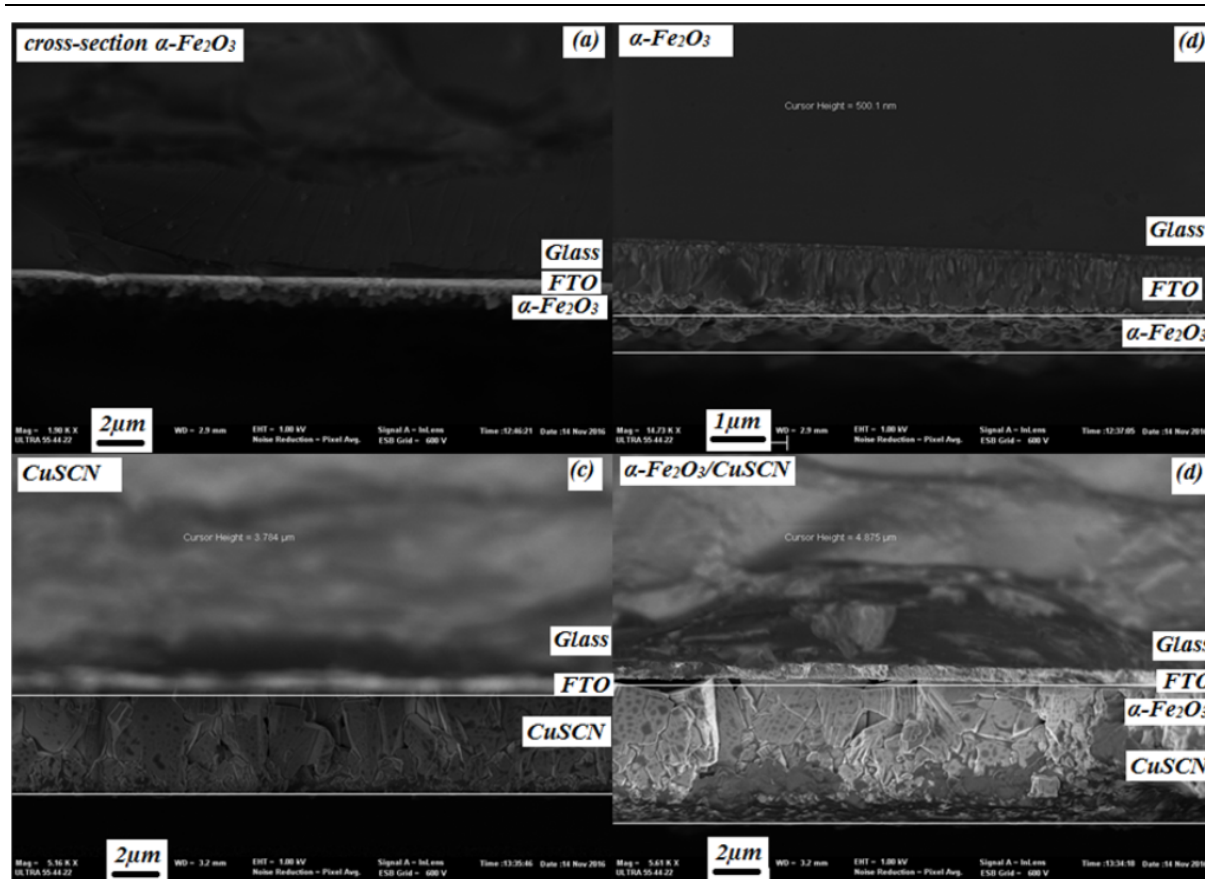
Figure 5: Vertical cross section of (a-b) α-Fe_2O_3, (c) CuSCN and (d) heterojunction thin films.

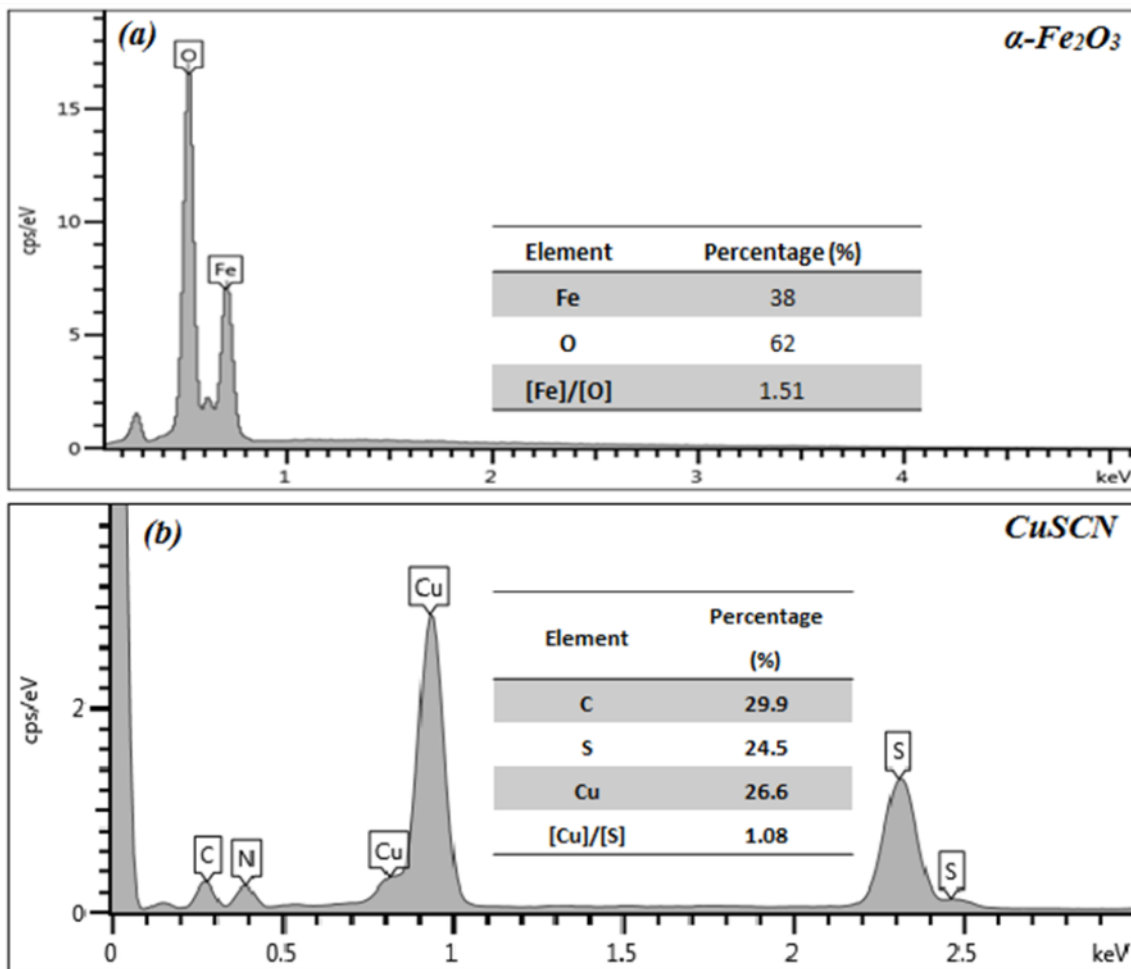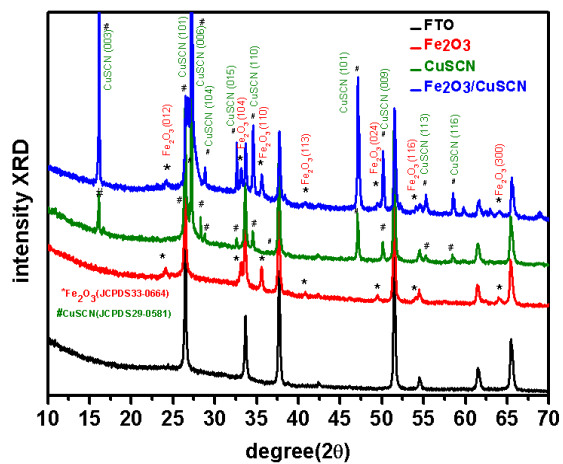Figure 6: Figure 6: (a) EDX spectrum for α-Fe_2O_3, (b) EDX spectrum for CuSCN thin films.

Figure 7: XRD spectra of FTO, α-Fe_2O_3, CuSCN and the Fe_2O_3/CuSCN bilayer.
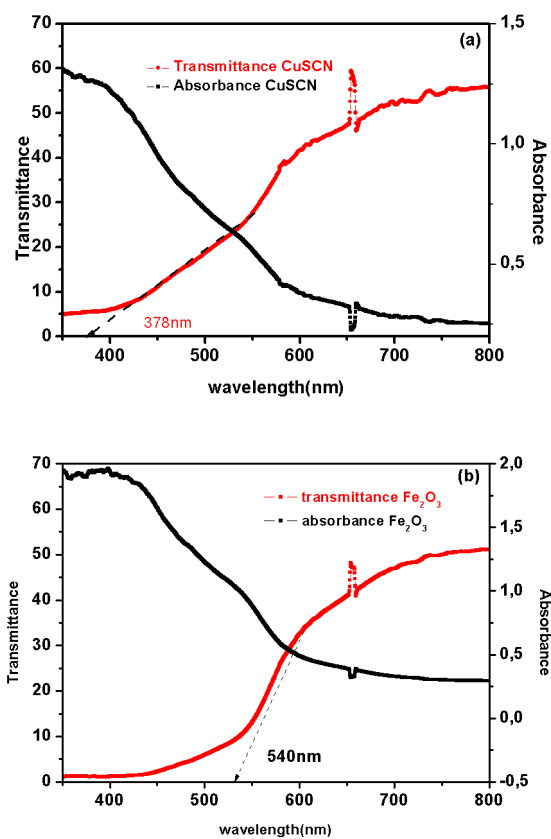
Figure 8: Transmittance and absorbance spectra of CuSCN (a) and α-Fe_2O_3 (b).

Figure 9: Tauc plot of CuSCN and α-Fe_2O_3.

Figure 10: PL spectrum of α-Fe_2O_3, CuSCN and Fe_2O_3/CuSCN.

Figure 11: (a) Energy band diagram of α-Fe_2O_3 and CuSCN before and after the formation p-n junction (b) schematic energy band diagram of the α-Fe_2O_3 and CuSCN heterojunction with the band bending and alignment due to the solution.

Figure 12: I-V characteristics of the α-Fe_2O_3 and CuSCN electrodein dark and illumination (0 V-0.8 V).

Figure 13: (a) Photocurrent intensity for α-$Fe_2O_3$and α-Fe_2O_3/CuSCN electrodes under on/off illumination, measured in 1M NaOH electrolyte under a bias potential of +0.1 V, (b) Time dependence of the photocurrent intensities for α-$Fe_2O_3$and α-Fe_2O_3/CuSCN electrodes under successive illumination cycles and (c) Time dependence of the photocurrent intensities for α-Fe_2O_3/CuSCN electrode under on/off illumination cycles (white light and λ >400 nm).

Figure 14: Mott–Schottky plot for (a) α-Fe_2O_3 (b) CuSCN (c) α-Fe_2O_3 /CuSCN.

Figure 1: Schematic cross-sectional view of heterojunction: FTO glass, compact α-Fe₂O₃, and

CuSCN (HTM).

| *Figure 2.a: Linear sweep voltammetry of Fe₂O₃ precursor solution in the range of -1V to 1V on the indium fluoride oxide electrode at a rate 50mVs⁻¹.* | *Figure 2.b: Linear sweepvoltammetry of CuSCN precursor solution in the range of -0.8V to 0.6V at a rateof 200 mVs⁻¹.* |

Figure 3: Chronoamperometry of CuSCN with a Cu: SCNratio of 1:1.5.
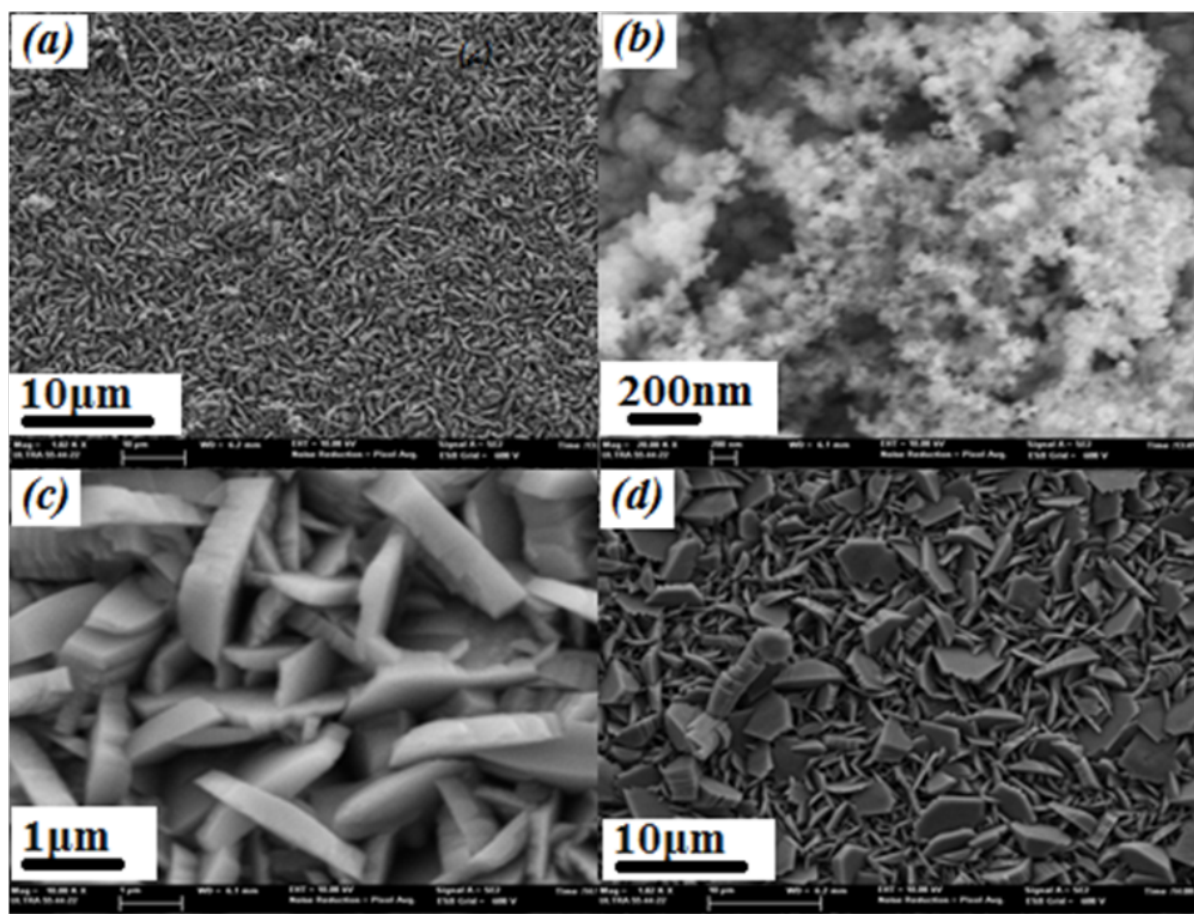
Figure 4: FESEM images for (a) CuSCN (b) α-Fe₂O₃(c) α-Fe₂O₃/CuSCN (1μm) (d) α-Fe₂O₃/CuSCN (10μm).

Figure 5: Vertical cross section of (a-b)α-Fe$_2$O$_3$, (c) CuSCN and (d) heterojunction thin films.

Figure 6: (a) EDX spectrum for α-Fe₂O₃, (b)EDX spectrum for CuSCN thin films.

*Figure 7: XRD spectra of FTO,α-Fe₂O₃, CuSCN andthe*Fe₂O₃/CuSCN bilayer.

Figure 8: Transmittance and absorbance spectra of CuSCN (a) and α-Fe₂O₃ (b).
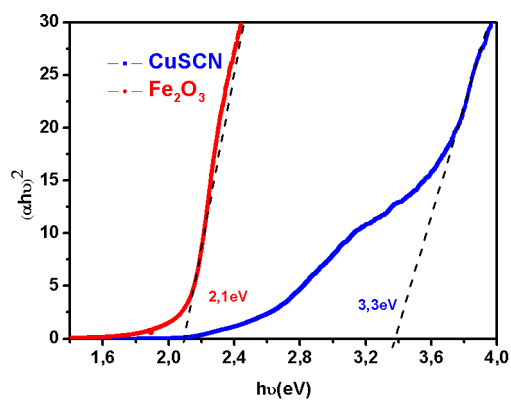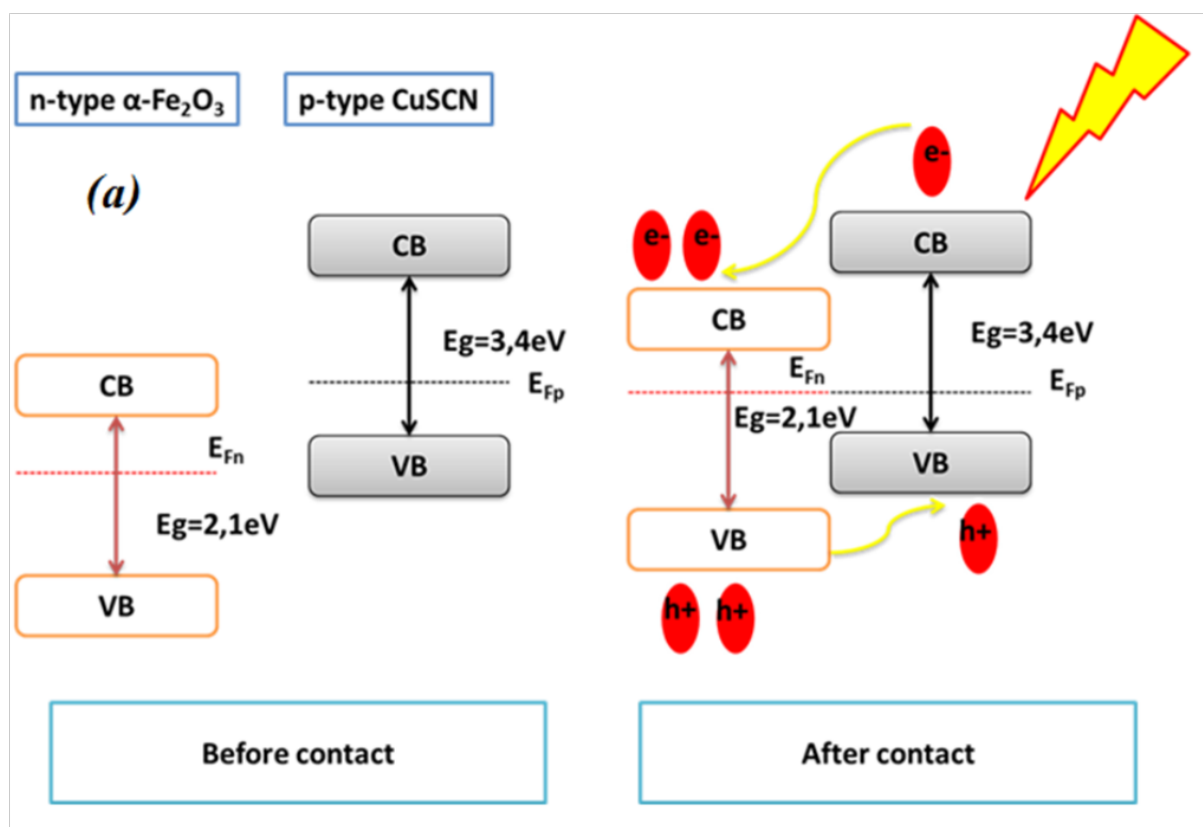

Figure 9: Tauc plot of CuSCN and α-Fe₂O₃.
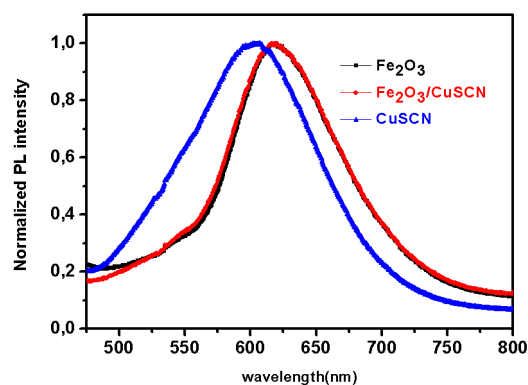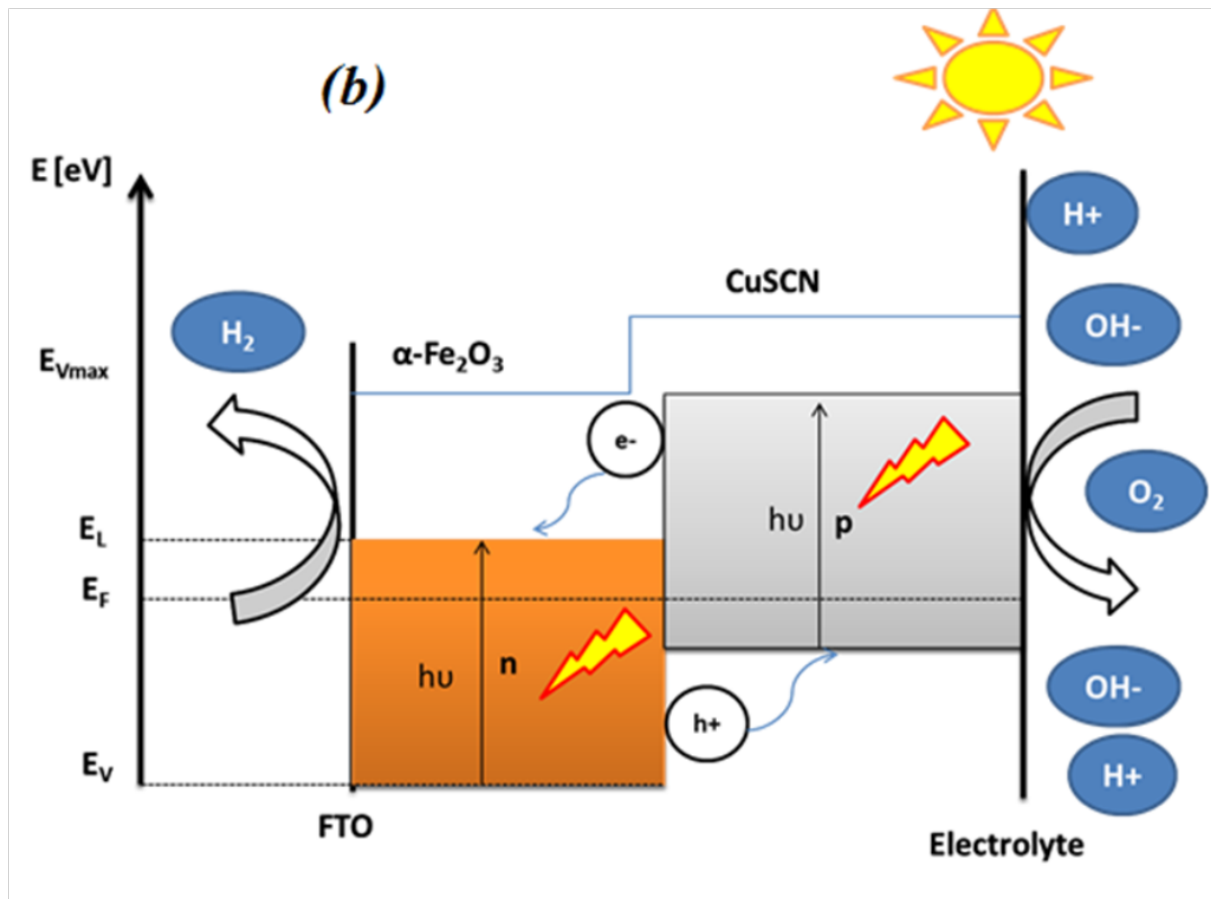
Figure 10:PL spectrum of α-Fe₂O₃, CuSCN and Fe₂O₃/CuSCN.

Figure 11: (a) Energy band diagram of α-Fe₂O₃ and CuSCN before and after the formation p-n junction (b) schematic energy band diagram of the α-Fe₂O₃ and CuSCN heterojunction with the band bending and alignment due to the solution.
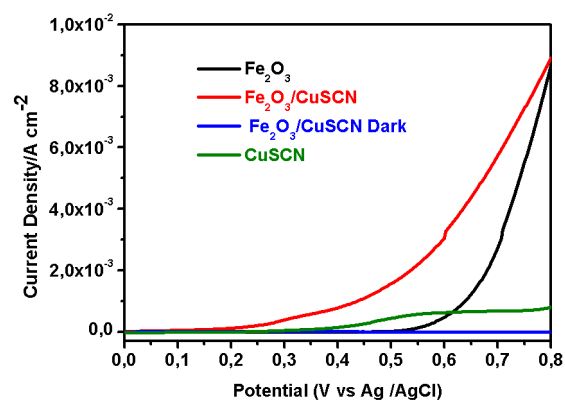

Figure 12: I-V characteristics of the α-Fe₂O₃, CuSCN and Fe₂O₃/CuSCN electrodes in the dark and under illumination.

Figure 13: (a) Photocurrent intensity for α-Fe₂O₃ and α-Fe₂O₃/CuSCN electrodes under on/off illumination, measured in 1M NaOH electrolyte under a bias potential of +0.1 V, (b) Time dependence of the photocurrent intensities for α-Fe₂O₃ and α-Fe₂O₃/CuSCN electrodes under successive illumination cycles and (c) Time dependence of the photocurrent intensities for α-Fe₂O₃/CuSCN electrode under on/off illumination cycles (white light and λ >400 nm).
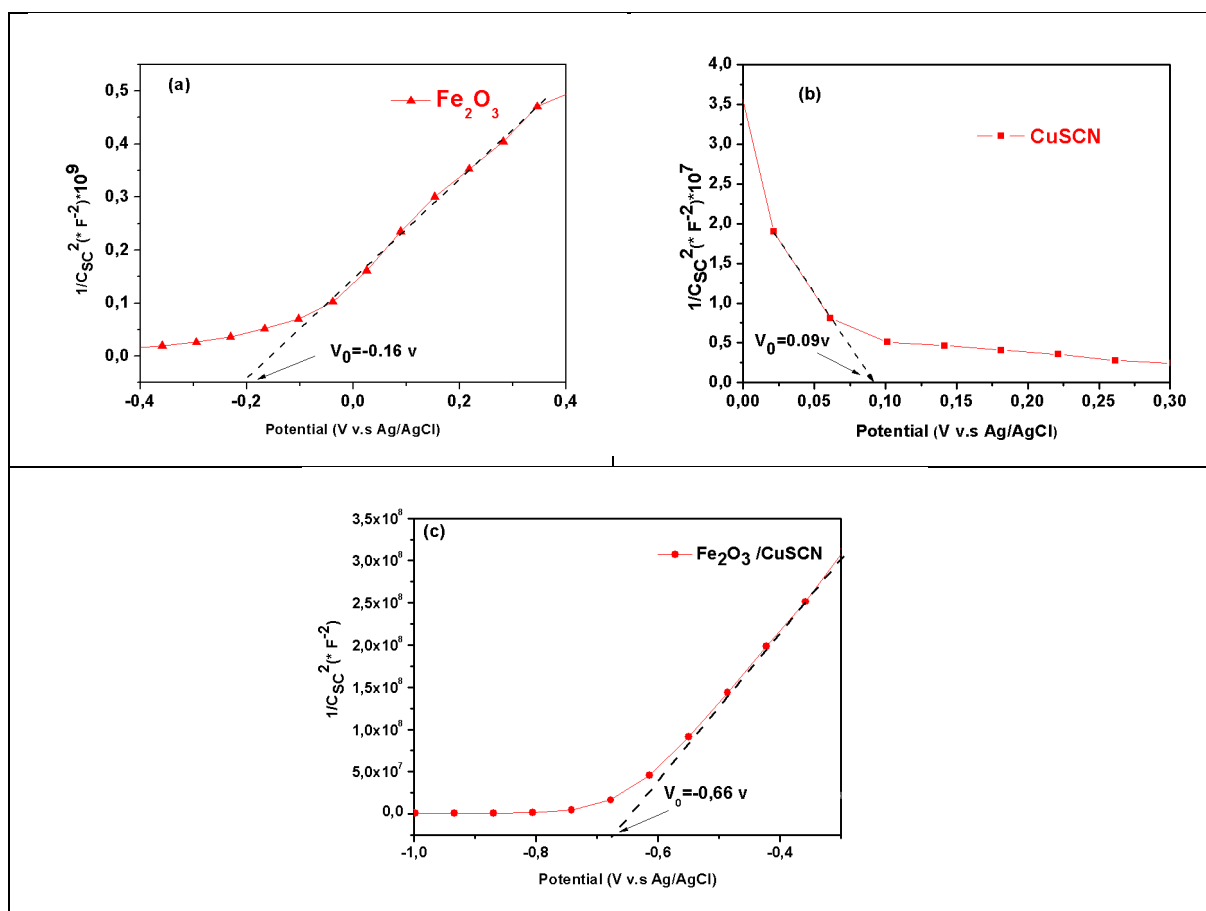
Figure 14: Mott–Schottky plot for (a) α-Fe₂O₃, (b) CuSCN, (c) α-Fe₂O₃/CuSCN.

Table Captions

Table I: Hematite-based heterostructures including fabrication methods, suggested charge transfer and photoelectrochemical characteristics.

Heterostructure	Fabrication method	Suggested charge transfer		Photoelectrochemistry	Ref.
		Electron	**Hole**		
$WO_3/\ \alpha$-Fe_2O_3	Sol–gel	$WO_3 \rightarrow \alpha$-Fe_2O_3	None	Photocurrent: 22 μAcm^{-2} at 0.8V vs. Ag/AgCl (500 W Xe lamp) lec- trolyte: 0.2 M Na_2SO_4 (pH = 7.5)	[19]
$WO_3/\ \alpha$-Fe_2O_3	Spin coating and Spray pyrolysis	None	None	Photocurrent: 22 $mAcm^{-2}$ at 0.8V vs. Ag/AgCl; electro- lyte: 0.05 M PBS (pH = 7)	[20]
ZnO/α-Fe_2O_3	Hydrothermal and spin coating	α-Fe_2O_3 $\rightarrow ZnO$	$ZnO \rightarrow \alpha$-Fe_2O_3	Photocurrent:1.6mA cm^{-2} at 0.6V vs. Ag/AgCl; electrolyte:1 M NaOH	[21
α-Fe_2O_3 /Gr/BiV_{1-x} Mo_xO_4	Hydrothermal and spin coating	$BiV_{1-x}Mo_xO_4 \rightarrow \alpha$-$Fe_2O_3$	α-Fe_2O_3 $\rightarrow BiV_{1-x}$ Mo_xO_4	Photocurrent: 0.39 mA cm^{-2} at 1.5 V vs. RHE (64 mW cm^{-2} $\lambda > 420$ nm); electrolyte: 0.01 M Na_2SO_4	[22]
α-$Fe_2O_3/ZnFe_2O_4$	Spin coating	$ZnFe_2O_4 \rightarrow \alpha$-$Fe_2O_3$	α-Fe_2O_3 $\rightarrow ZnFe_2O_4$	Photocurrent: 0.44 mA cm^{-2} at 0.2 V vs. Ag/AgCl; electrolyte: 0.1 M glucose and 0.5 M NaOH (pH = 13.0)	[23]
α-Fe_2O_3: Ti/$ZnFe_2O_4$	Hydrothermal and surface treatment	$ZnFe_2O_4 \rightarrow \alpha$-$Fe_2O_3$: Ti	α-Fe_2O_3: Ti $\rightarrow ZnFe_2O_4$	Photocurrent: 0.3 mA cm^{-2} at 1.4 V vs. RHE; electrolyte: 1 M KOH	[24]
α-Fe_2O_3: Co/$MgFe_2O_4$	Hydrothermal and wet impregnation	$MgFe_2O_4 \rightarrow \alpha$-$Fe_2O_3$: Co	α-Fe_2O_3: Co $\rightarrow MgFe_2O_4$	Photocurrent: 3.34 mA cm^{-2} at 1.4 V vs. RHE; electrolyte: 0.01 M Na_2SO_4	[25]
p-$CaFe_2O_4$/n-Fe_2O_3	Hydrothermal and two-step annealing	p-$CaFe_2O_4 \rightarrow$ n-Fe_2O_3	n-Fe_2O_3 $\rightarrow$ p-$CaFe_2O_4$	Photocurrent: 0.53 mA cm^{-2} at 1.23 V vs. RHE; electrolyte: 1.0 M KOH (pH = 13.9)	[26]
α-Fe_2O_3: Ti/Cu_2O	Spray pyrolysis	$Cu_2O \rightarrow \alpha$-Fe_2O_3: Ti	α-Fe_2O_3: Ti $\rightarrow$ Cu_2O	Photocurrent: 2.60 mA cm^{-2} at 0.95 V vs. SCE (Xe lamp, 150 mW cm^{-2}); electrolyte: 0.1 M NaOH	[27]
α-Fe_2O_3/CuSCN	Electrodeposition	$CuSCN \rightarrow \alpha$-Fe_2O_3	α-$Fe_2O_3 \rightarrow$ CuSCN	Photocurrent: 2.90 mA cm^{-2} at 0.59 V vs. Ag/AgCl. (Xe lamp: 150 W); electrolyte 0.1 M NaOH (pH = 13.9)	**our work**